Energy Based Multiresolution Analysis of FBG-Measured Strain Responses for Void Detection in Curved Pressure Vessel Structures Under Guided-Wave Excitation

Napoleon Kuebutornye , Ziping Wang * , Xilin Wang , Qingwei Xia , Alfredo Güemes , Antonio Fernández Lopez

Posted Date: 1 April 2026

doi: 10.20944/preprints202604.0067.v1

Keywords: structural health monitoring; guided-wave excitation; fiber bragg grating sensors; multiresolution wavelet analysis; energy-based diagnostics

 doi:10.20944/preprints202604.0067.v1

Article

Energy Based Multiresolution Analysis of FBG-Measured Strain Responses for Void Detection in Curved Pressure Vessel Structures Under Guided-Wave Excitation

Napoleon Kuebutornye [1], Ziping Wang [1,*], Xilin Wang [2], Qingwei Xia [1], Alfredo Güemes [3] and Antonio Fernández-López [3]

[1] Faculty of Civil Engineering and Mechanics, Jiangsu University and National Center for International Research on Structural Health Management of Critical Components, 212013 Zhenjiang, China

[2] Institute of Ocean Engineering, Shenzhen International Graduate School, Tsinghua University, Shenzhen 518055, China

[3] Department of Aeronautics, Polytechnic University of Madrid, 28040 Madrid, Spain

* Correspondence: wzpxx2004@126.com

Abstract

Reliable detection of internal defects in pressure vessel structures remains essential for structural safety and condition based maintenance. This study presents a low-complexity structural health monitoring framework based on fiber Bragg grating (FBG) sensing and multiresolution wavelet analysis for void detection in curved pressure vessel structures under guided-wave excitation. Guided waves are introduced using piezoelectric actuators, while the FBG sensors capture the resulting strain-induced wavelength variations. Due to the limited bandwidth of the optical interrogator, the recorded signals represent the strain envelope response associated with guided-wave interaction rather than the resolved ultrasonic carrier waveform. To characterize defect-induced changes, the acquired signals are analyzed using continuous wavelet transform (CWT) for time frequency interpretation, and discrete wavelet transform (DWT) and wavelet packet transform (WPT) for energy-based multiresolution feature extraction. Experimental results show that void defects lead to consistent redistribution of wavelet-domain energy and increased non-stationarity in the measured strain responses. These trends are further supported by finite element simulations, which reproduce similar energy redistribution patterns between intact and damaged cases. The proposed framework provides a physically interpretable and computationally efficient approach for defect detection using low-bandwidth FBG sensing, without reliance on high-speed acquisition or data-intensive learning models. The results demonstrate the feasibility of using energy-based multiresolution analysis of FBG strain signals for practical and scalable structural health monitoring of pressure vessel systems.

Keywords: structural health monitoring; guided-wave excitation; fiber bragg grating sensors; multiresolution wavelet analysis; energy-based diagnostics

1. Introduction

Early approaches to the structural health monitoring (SHM) of pressure vessels (PVs), as illustrated in Figure 1a, primarily relied on visual inspection conducted by engineers and skilled personnel during construction and early service stages. Although widely adopted, visual inspection is inherently subjective and limited to surface visible defects, making it unsuitable for early damage detection or continuous monitoring of safety critical pressure vessel structures (PVSs). The 1950s to 1960s marked a major transition with the development of non-destructive testing and evaluation

 doi:10.20944/preprints202604.0067.v1

(NDT/E) techniques aimed at detecting subsurface material and structural damage, including fatigue cracking in metallic components and delamination in composite structures [1]. These methods significantly improved inspection reliability; however, they remained periodic, labor-intensive, and dependent on operator expertise.

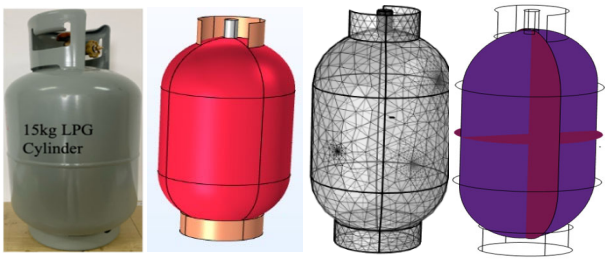

Figure 1. Experimental and numerical configuration of the pressure vessel structure (a) 15 kg LPG pressure vessel used in the experiment, (b) geometry, (c) mesh, and (d) guided-wave propagation model.

In the 1980s, acoustic emission (AE) techniques emerged as a promising approach for PV monitoring. Ohtsuka et al. [2] demonstrated the feasibility of using AE signals for defect detection in pressure vessels, enabling continuous monitoring of damage evolution. To enhance robustness under noisy operating conditions, adaptive signal processing techniques such as adaptive singular value decomposition (ASVD) were later introduced [3,4]. Subsequent studies further advanced AE-based monitoring, including investigations of deformation mechanisms in composite pressure vessels [5] and crack growth monitoring in metallic structures [6–8], establishing AE as a viable technique for in situ structural assessment. During the 1990s, research emphasis shifted toward guided ultrasonic wave-based SHM, accompanied by advances in signal processing and early networked monitoring systems. Guided waves gained prominence due to their high sensitivity to structural discontinuities and their ability to inspect large areas using a limited number of sensors [9,10]. These characteristics significantly improved detection capability and supported the development of real-time structural monitoring approaches.

In the 2000s and beyond, substantial technological progress further expanded SHM capabilities. Research extended toward Internet of Things (IoT) enabled monitoring systems, facilitating real-time data acquisition, transmission, and analysis [11,12]. Parallel developments focused on diagnostic measurement, information condensation, and damage identification across a wide range of engineering structures, including aircraft, wind energy systems, bridges, offshore platforms, and mechanical components [13,14]. In addition, guided ultrasonic waves were increasingly applied to composite and hybrid structures for detecting defects such as disbonding and delamination through advanced modeling and signal processing techniques [15]. Guided wave-based SHM methods are commonly categorized into passive and active approaches. Passive methods, such as AE, rely on damage induced acoustic activity but often suffer from limited repeatability and controllability. In contrast, active methods employ controlled excitation, enabling repeatable measurements, improved signal interpretation, and enhanced defect localization. As a result, active guided wave techniques are widely regarded as effective solutions for large-area monitoring of pressure vessel structures [16].

Despite these advances, several critical challenges remain. Many guided-wave based SHM systems rely on dense sensor networks, resulting in increased system complexity, higher installation costs, and reduced practicality for large-scale industrial deployment [17–19]. Furthermore, single-sensor sensing strategies, particularly those based on FBG sensors, remain underexplored for complex curved geometries such as pressure vessels, with most existing studies focusing on flat plates or simple beam structures [20–22]. In addition, existing studies often emphasize qualitative time-frequency visualization, while quantitative and physically interpretable multiresolution energy-based diagnostics are rarely integrated into a unified analytical framework for defect characterization [23–25]. Moreover, void detection in curved pressure vessel geometries has received relatively

 doi:10.20944/preprints202604.0067.v1

limited attention compared to planar structures, despite its direct relevance to real world applications [26,27]. These limitations collectively hinder the scalability, affordability, and practical adoption of advanced SHM frameworks in industrial environments [28–30].

Unlike conventional ultrasonic guided-wave SHM approaches that rely on high-frequency waveform acquisition, this study focuses on the strain-envelope response captured by a low-bandwidth FBG interrogator. The sensing system does not resolve the ultrasonic carrier waveform; instead, it records the effective strain modulation induced by guided-wave excitation and its interaction with structural discontinuities. Consequently, the analysis does not rely on ultrasonic phase, time-of-flight, or high-frequency spectral content, but rather on energy redistribution patterns and non-stationary features observable within the interrogator bandwidth. This distinction ensures consistency between the sensing mechanism and the adopted signal processing framework [31,32].

Therefore, this study makes three main contributions. First, it establishes a sensing paradigm in which low-bandwidth FBG interrogators are used to capture strain-envelope responses induced by guided-wave excitation, eliminating the need for high-speed ultrasonic acquisition systems. Second, it introduces a unified multiresolution energy-based diagnostic framework that integrates continuous wavelet transform (CWT)-based time-frequency interpretation with discrete wavelet transform (DWT) and wavelet packet transform (WPT) energy features, enabling physically interpretable characterization of defect-induced signal changes. Third, the proposed framework is validated on a curved pressure vessel geometry, demonstrating that meaningful defect-sensitive features can be extracted from single-channel FBG measurements while reducing sensing complexity.

2. Experimental Methodology and Specimen Description

Experiments were conducted on a 15 kg liquefied petroleum gas (LPG) steel cylinder [33], selected as a representative curved, thin-walled pressure vessel structure (PVS) used in practical applications. Two structural conditions were investigated: (i) a no-void condition representing the intact (healthy) state, and (ii) a void condition in which an artificial defect was introduced to create a controlled internal discontinuity. This design enables direct comparison of strain responses under identical excitation and acquisition conditions. Two FBG sensors (FBG1 and FBG2) were surface-mounted on the external wall of the cylinder using high-strength epoxy to ensure effective strain transfer. Guided-wave excitation was generated using two PZT-5H piezoelectric transducers. Two measurement configurations were considered to examine sensitivity under different wave paths. In Study 1, PZT1 acted as the actuator and FBG1 as the receiver; in Study 2, PZT2 acted as the actuator and FBG2 as the receiver, as illustrated in Figure 2. Each configuration represents a single-sensor measurement scenario under a distinct actuator sensor path.

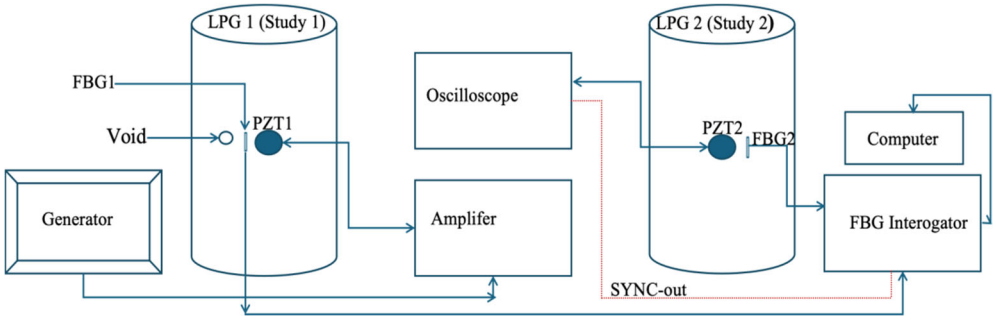

Figure 2. Schematic diagram of experimental sensor configuration and instrumentation setup.

The PZT actuators were driven using a high-voltage amplifier (Aigtek ATA-2021H). Excitation signals and trigger timing were monitored using a Tektronix 4-Series mixed-signal oscilloscope. The FBG wavelength responses were recorded using a Micron Optics SM130 optical interrogator operating at a sampling rate of 2 kHz.

 doi:10.20944/preprints202604.0067.v1

2.1. Excitation and Acquisition Settings

Guided-wave excitation was applied using a five-cycle tone-burst signal with a central frequency of 100 kHz. Each experimental run was recorded for 10 s, during which the FBG interrogator continuously measured wavelength shifts induced by the dynamic strain field on the vessel surface. Due to the limited sampling rate of the interrogator (2 kHz), the recorded FBG signals do not resolve the high-frequency ultrasonic carrier waveform. Instead, the measurements represent the strain-envelope response associated with guided-wave excitation and its interaction with the structure. The acquired signals therefore reflect low-frequency modulation behavior induced by repeated high-frequency actuation and wave structure interaction effects. Accordingly, the subsequent analysis focuses on the temporal evolution and multiresolution characteristics of the recorded strain signals, rather than on ultrasonic phase, cycle-level waveform reconstruction, or high-frequency time-of-flight estimation. To ensure consistency across repeated experiments, the acquisition window was aligned with the excitation sequence. Trigger alignment was verified by routing the interrogator SYNC-out signal to the oscilloscope auxiliary input, as shown in Figure 3. This configuration was used solely for verification of repeatability and timing consistency; no phase-locked or waveform-level synchronization was required for the adopted analysis framework.

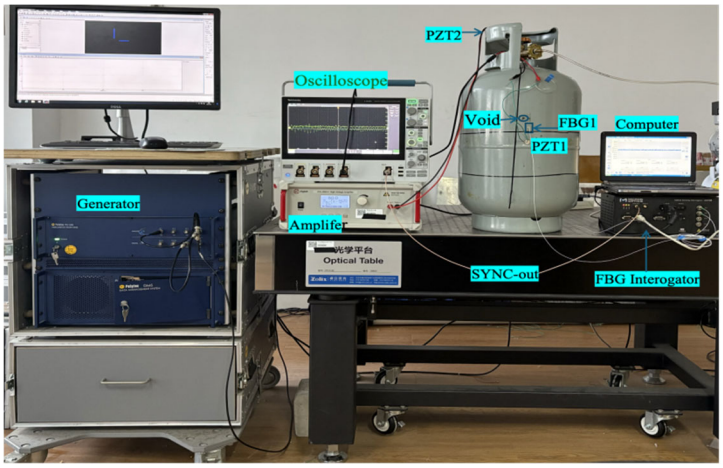

Figure 3. Experimental setup for guided-wave excitation and FBG signal acquisition.

The acquired data were stored as plain-text wavelength measurements for each experimental condition (FBG1_void, FBG1_novoid, FBG2_void, and FBG2_novoid).

Prior to feature extraction, all signals were preprocessed to reduce baseline drift and ensure comparability across runs. This preprocessing included mean removal, detrending, and amplitude normalization through standardization.

2.2. Numerical Simulation

A finite element (FE) model was developed to support the physical interpretation of the experimentally observed strain responses, particularly the redistribution of signal energy associated with defect presence. The objective of the simulation was not to construct a fully predictive digital twin, but rather to reproduce the qualitative differences between intact and voided conditions under consistent excitation settings. A three dimensional model of the LPG steel cylinder was constructed to replicate the experimental geometry and material behavior as shown in Figure 1b. The vessel wall was modeled as a linear elastic, isotropic material. A void type defect was introduced as a localized volumetric discontinuity at the same region considered in the experimental setup in Figure 1c, enabling direct comparison between the intact and defective cases while maintaining identical boundary conditions.

Guided-wave excitation was modeled using a surface mounted PZT-5H actuator represented through fully coupled piezoelectric constitutive relations. A five-cycle tone-burst signal at 100 kHz

 doi:10.20944/preprints202604.0067.v1

was applied as a voltage boundary condition to match the experimental excitation as indicated Figure 1d. The simulation was solved using a coupled electromechanical formulation, and absorbing boundary conditions were implemented to minimize non-physical reflections from model boundaries.

To emulate the sensing process, virtual FBG measurement points were defined at locations corresponding to the physical sensor placements. The axial strain time histories extracted at these locations were used as simulation outputs. These strain signals serve as numerical analogues of the experimentally measured wavelength shifts (after preprocessing) and were processed using the same multiresolution analysis framework (CWT, DWT, and WPT). This ensures consistency between experimental and numerical signal representations.

Two types of outputs were used to support interpretation. First, the spatial distribution of electric potential on the actuator surface, Figure 4a provides a qualitative validation of the applied excitation and electromechanical coupling. Second, the extracted strain time histories at the virtual probe locations also in Figure 4(b) exhibit spatial variability in response amplitude and temporal behavior. Some locations show stronger dynamic responses due to wave propagation and defect interaction, while others exhibit weaker responses, indicating reduced coupling with the wavefield. These variations support the use of localized strain measurements as defect-sensitive observables and are consistent with the experimentally observed energy redistribution patterns.

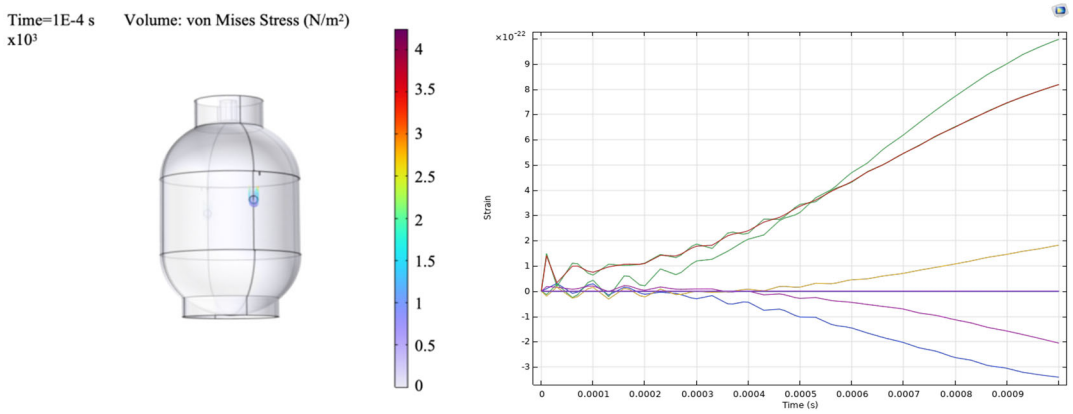

Figure 4. (a) Electric potential distribution on the vessel surface under PZT excitation. (b) Extracted axial strain time histories at selected virtual probe locations.

2.3. Mathematical Theories and Principles of the Study

This section outlines the theoretical foundations of the multiresolution wavelet framework used to analyze strain responses measured by FBG sensors under guided-wave excitation. The focus is on time-frequency representation and energy-based diagnostics, which enable characterization of defect induced changes in non-stationary signals.

2.4. FBG-Based Strain Response Under Guided-Wave Excitation

Guided-wave excitation induces a transient strain field on the surface of the pressure vessel. This strain causes a shift in the Bragg wavelength of the FBG sensor. Under isothermal conditions, the relationship between axial strain and wavelength shift is expressed as:

$$\Delta\lambda_B = \lambda_B(1 - p_e)\varepsilon \quad (1)$$

where $\Delta\lambda_B$ is the Bragg wavelength shift, λ_B is the initial Bragg wavelength, *Pe* is the effective photoelastic coefficient, and ε is the axial strain. In this study, the recorded FBG signal represents the strain envelope response associated with guided-wave excitation.

 doi:10.20944/preprints202604.0067.v1

2.5. Continuous Wavelet Transform (CWT)

Guided-wave induced strain responses are inherently non-stationary due to dispersion, mode interaction, and defect-induced scattering. To capture these characteristics, the continuous wavelet transform (CWT) is employed. For a signal *x(t)*, the CWT is computed as [34]:

$$W(a,B)=\int_{-\infty}^{\infty}x(t)\psi^{*}\left(\frac{t-b}{a}\right)dt \tag{2}$$

where *a* is the scale parameter related to frequency, *b* is the time translation parameter, $u(\cdot)$ is the mother wavelet, and $(\cdot)^{*}$ denotes complex conjugation. The magnitude of the wavelet coefficients provides a time-frequency representation (scalogram), which enables visualization of energy distribution, temporal localization, and non-stationary behavior associated with defect presence.

2.6. Discrete Wavelet Transform (DWT)

To obtain compact and quantitative features, the discrete wavelet transform (DWT) is used to decompose the signal into multiple resolution levels corresponding to different frequency bands [35]:

$$x(t)=\sum_{k}A_{J,k\phi J,k}(t)+\sum_{j=1}^{J}\sum_{k}D_{j,k\psi j,k}(t) \tag{3}$$

where $A_{J,K}$ are approximation coefficients at level *J*, $D_{j,k}$ are detail coefficients at level $j, and \phi, \psi$ denote the scaling and wavelet functions respectively.

$$E_{j}=\sum_{k}\left|D_{j,k}\right|^{2} \tag{4}$$

To allow comparison across signals, the energy is normalized:

$$\tilde{E}_{j}=\frac{E_{j}}{\sum_{j=1}^{J}E_{j}} \tag{5}$$

Changes in normalized energy distribution reflect defect-induced modifications in the strain response.

2.7. Wavelet Packet Transform (WPT) and Node Energy

The WPT provides finer frequency resolution by decomposing both approximation and detail components. For a wavelet packet node, the energy is defined as:

$$E_{n}=\sum_{k}\left|C_{n,k}\right|^{2} \tag{6}$$

where $C_{n,k}$ are the wavelet packet coefficients. The normalised energy is given by:

$$\tilde{E}_{n}=\frac{E_{n}}{\sum_{n=1}^{N}E_{n}} \tag{7}$$

where *N* is the number of terminal nodes. This representation is useful for detecting fine-band energy shifts that can occur when guided waves interact with localised voids [36].

2.8. Energy Based Damage Interpretation

Void defects influence guided-wave propagation through scattering, attenuation, and mode interaction. In the proposed framework, these effects manifest as redistribution of signal energy across wavelet scales and frequency bands. CWT provides qualitative insight into time-frequency behavior, while DWT and WPT offer physically interpretable energy-based features. Together, these methods enable multiresolution diagnostic framework suitable for analyzing FBG-measured strain-envelope responses in pressure vessel structures.

 doi:10.20944/preprints202604.0067.v1

3. Results and Discussion

3.1. Preprocessed FBG Strain Responses

Figure 5 provides a comparison of the preprocessed FBG wavelength responses under no-void and void conditions for the two sensing locations. Although the raw traces remain highly oscillatory, differences in temporal structure become more apparent in the corresponding envelope responses. In particular, the void condition exhibits stronger local fluctuations and altered envelope patterns relative to the no-void state. These signal-level differences provide preliminary evidence that the defect affects the measured strain response and aided the subsequent use of CWT, DWT, and WPT for more systematic time-frequency and energy-based characterization.

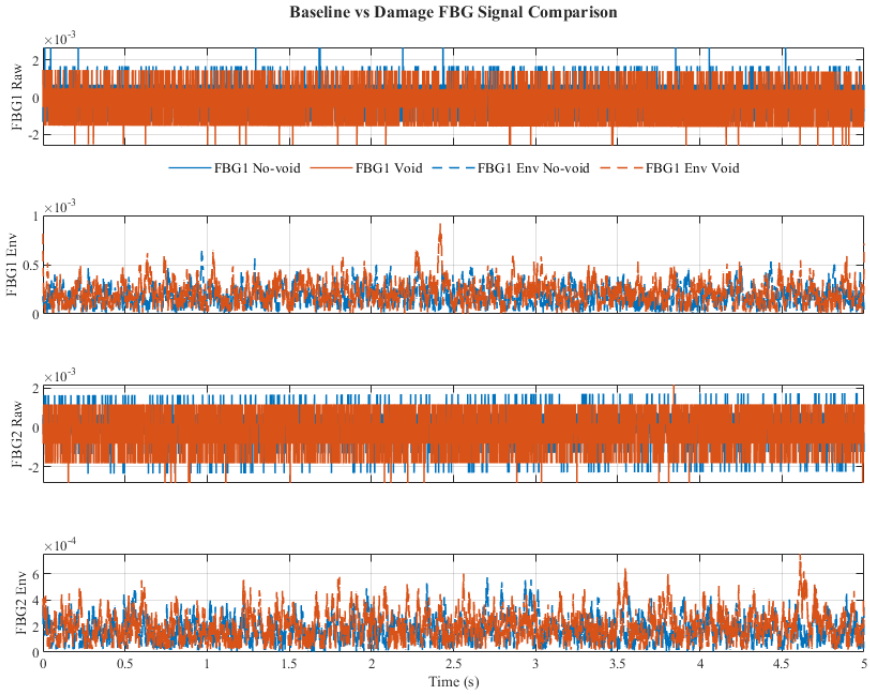

Figure 5. Comparison of preprocessed FBG strain responses under no-void and void conditions at the two sensing locations (a) FBG1 preprocessed signal, (b) FBG1 envelope response, (c) FBG2 preprocessed signal, and (d) FBG2 envelope response.

3.2. Time-Frequency Characteristics from CWT Scalograms

Figure 6a–d present the logarithmic continuous wavelet transform (CWT) scalograms of the measured FB wavelength responses for the no-void and void conditions at the two sensing locations, FBG1 and FBG2. The resulting time-frequency maps show broadband signal components within the bandwidth of the optical interrogator. Under the no-void condition, the energy distribution remains relatively smooth and temporally stable, indicating a more repeatable strain-envelope response under nominal wave propagation conditions. In contrast, the void condition exhibits increased non-stationarity, characterized by localized energy concentrations and intermittent patches distributed across multiple frequency bands. These features are consistent with defect-induced modifications in the measured response, where interaction between the guided-wave field and the void introduces additional scattering, attenuation, and mode interaction, leading to time varying redistribution of signal energy.

 doi:10.20944/preprints202604.0067.v1

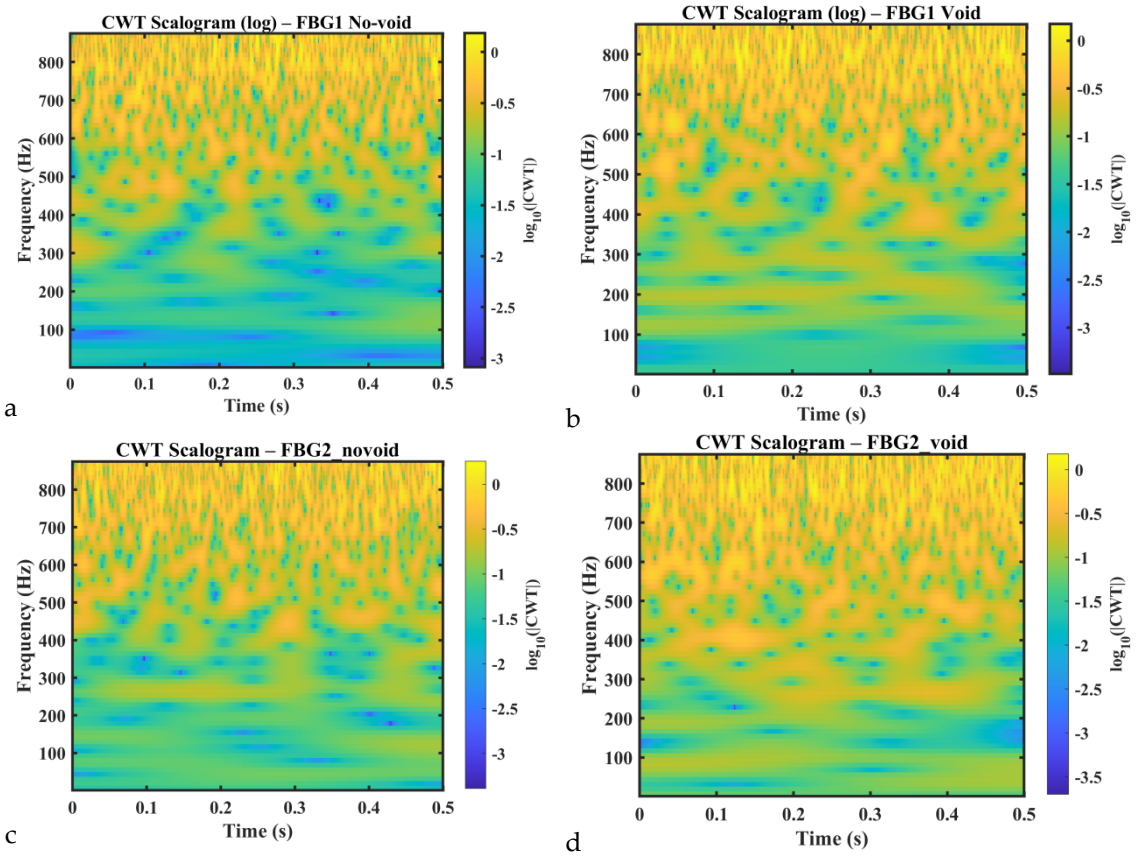

Figure 6. ((a,b, c,d). CWT scalograms of the FBG wavelength responses for the no-void and void cases at the two sensing locations (FBG1 and FBG2).

A comparison of the two sensing locations further shows that the magnitude and visibility of these perturbations differ between FBG1 and FBG2. This difference reflects the combined effects of wave path, structural curvature, and local strain coupling at each sensing position. In the present dataset, the void case measured at FBG2 exhibits more pronounced localized energy perturbations than the corresponding no-void case. This suggests that defect sensitivity is not governed solely by sensor proximity to the defect, but also by how scattered wave energy is redistributed along the curved vessel wall and coupled into the surface strain measured by the FBG sensor.

Overall, the CWT scalograms provide an interpretable view of damage related non-stationary behavior that is not readily visible in the raw wavelength traces. Although the CWT results are used here primarily for qualitative interpretation, they provide significant evidence that the void condition alters the time-frequency structure of the measured strain response and thereby implies the subsequent use of DWT- and WPT-based energy features for compact quantitative discrimination.

3.3. DWT Normalized Energy Distribution

Figure 7 shows the normalized discrete wavelet transform (DWT) energy distribution across five decomposition levels for FBG1 and FBG2 under the no-void and void conditions. In all cases, the majority of the signal energy is concentrated in the first two decomposition levels, indicating that the measured response is dominated by low-frequency components within the strain-envelope captured by the interrogator.

Relative to the intact state, the void condition exhibits a small but consistent redistribution of energy toward higher decomposition levels. Within the available measurement bandwidth, this trend indicates the presence of faster fluctuations and increased non-stationarity in the measured strain response. Such redistribution is consistent with defect-related scattering and mode interaction, which alter the temporal structure of the recorded signal even when the ultrasonic carrier itself is not directly resolved. The effect is more pronounced for the FBG2 configuration, where the higher-level

 doi:10.20944/preprints202604.0067.v1

energy content increases more noticeably in the void case. This observation supports the interpretation that damage sensitivity depends not only on sensor proximity, but also on wave path, structural curvature, and local strain coupling between the guided-wave field and the sensing location.

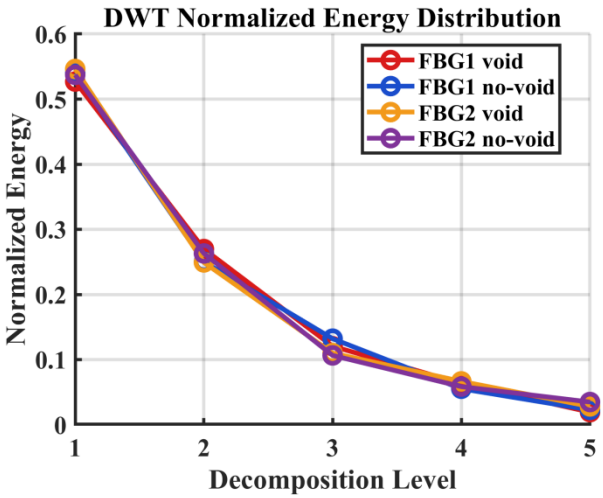

Figure 7. Normalized DWT energy distribution across five decomposition levels for FBG1 and FBG2 under void and no-void conditions.

Overall, the normalized DWT energy features provide a relatively interpretable indicators of structural condition. Because the features are normalized, they are less sensitive to absolute amplitude variation than raw time-domain measures, making them more suitable for consistent comparison under limited-data experimental conditions.

3.4. WPT Normalized Energy Distribution

Figure 8 presents the normalized wavelet packet transform (WPT) energy distribution across the terminal nodes for all experimental cases. Unlike the DWT, which provides a logarithmic frequency decomposition, the WPT decomposes both approximation and detail components, resulting in finer frequency partitioning. This enhanced resolution improves sensitivity to localized spectral changes associated with structural defects.

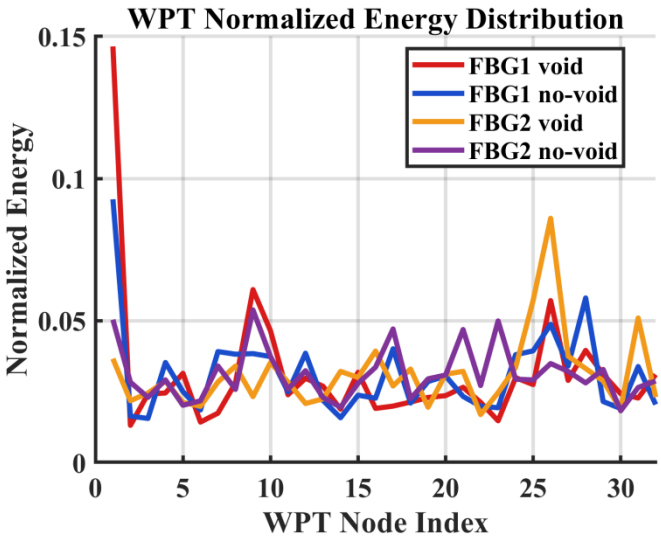

Figure 8. Normalized WPT node-energy distribution for FBG1 and FBG2 under void and no-void conditions.

 doi:10.20944/preprints202604.0067.v1

Across all cases, the first WPT node contains the largest proportion of the total energy. This can be attribeted to the measured FBG responses dominated by low-frequency strain-envelope content within the bandwidth of the interrogator. Beyond this dominant component, however, clear differences appear between the intact and defective states. The void condition can be seen to exhibit localized increases in normalized energy at specific node ranges, indicating redistribution of signal content across the available frequency bands. These changes are consistent with defect related scattering, attenuation, and mode interaction, which modify the structure of the measured response. By contrast, the no-void condition shows a comparatively smoother and more evenly distributed energy pattern, with fewer pronounced peaks across the terminal nodes. This suggests a more stable response under nominal wave propagation conditions and supports the interpretation that the observed node-level variations in the void case are defect sensitive rather than random fluctuations.

Overall, the WPT results significantly show that the presence of a void modifies the band-wise energy distribution in a way that is not fully captured by DWT alone. When combined with the qualitative interpretation provided by the CWT scalograms, the WPT node energies offer a compact, physically interpretable, and computationally efficient feature set for defect discrimination in curved pressure vessel structures.

3.5. Numerical Simulation Results

The numerical model was used to support the physical interpretation of the experimentally observed energy redistribution, rather than to reproduce absolute amplitudes or exact frequency values. Strain time histories were extracted at virtual probe locations corresponding to the experimental FBG positions, and the same multiresolution analysis framework was applied to the simulated responses, including CWT for time-frequency visualization and DWT/WPT for energy-based characterization.

Figure 9a,b show representative CWT scalograms obtained from the simulated strain responses for an intact case (FBG1 no-void) and a defective case (FBG2 void), respectively. In the intact condition, the scalogram exhibits a smoother and more stable time-frequency energy distribution, consistent with guided-wave propagation in the absence of a structural discontinuity. In contrast, the defective case shows attenuation and redistribution of energy, reflecting the influence of defect-induced scattering and mode interaction on the simulated strain response. The absolute frequency axes of the numerical scalograms should not be interpreted as directly equivalent to those of the experimental results, since they depend on discretization settings, numerical solver parameters, and modeling assumptions. The main point of comparison is therefore not absolute frequency alignment, but the relative change in the energy distribution between intact and voided conditions. In this respect, the simulation and experiment show the same qualitative trend that, represence a void modifies the temporal and spectral organization of the strain response and produces measurable redistribution of signal energy.

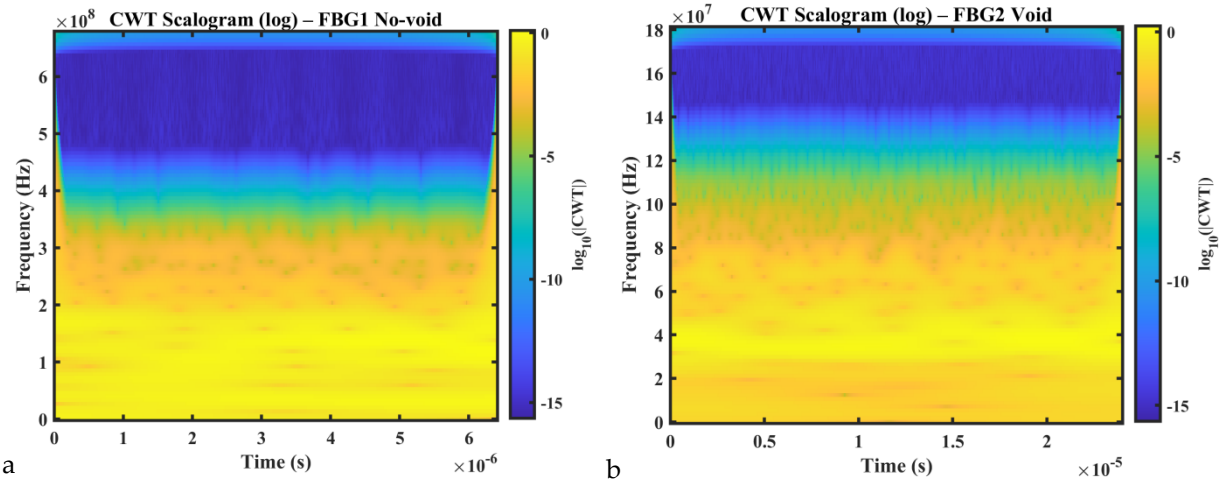

 doi:10.20944/preprints202604.0067.v1

Figure 9. Numerical CWT scalograms (log magnitude) obtained from simulated strain responses at virtual FBG locations: (a) FBG1 no-void (intact condition), (b) FBG2 void (defect condition).

Hence, the numerical results seek to reinforce the experimental interpretation by showing that the observed wavelet-energy changes are consistent with the expected physical effects of defect interaction. The agreement between simulation and experiment therefore can be seen supporting the use of multiresolution energy features as physically meaningful indicators of structural condition in the proposed sensing framework.

3.6. Simulated DWT and WPT Energy Features

To further quantify these observations, normalized DWT and WPT energy features were computed from the simulated strain responses. Figure 10a presents the WPT normalized node-energy distribution, while Figure 10b shows the normalized DWT energy across the decomposition levels. Showing consistence with the experimental results, the void condition exhibits a clearer redistribution of energy across wavelet bands compared with the intact condition. In particular, the damaged case shows a shift in energy concentration across selected nodes and levels, indicating that the presence of a void modifies the structure of the strain response in a manner that is detectable through compact multiresolution features. These results support the interpretation that defect-induced changes are not limited to simple amplitude reduction, but involve broader reorganization of the signal energy across scales and frequency bands.

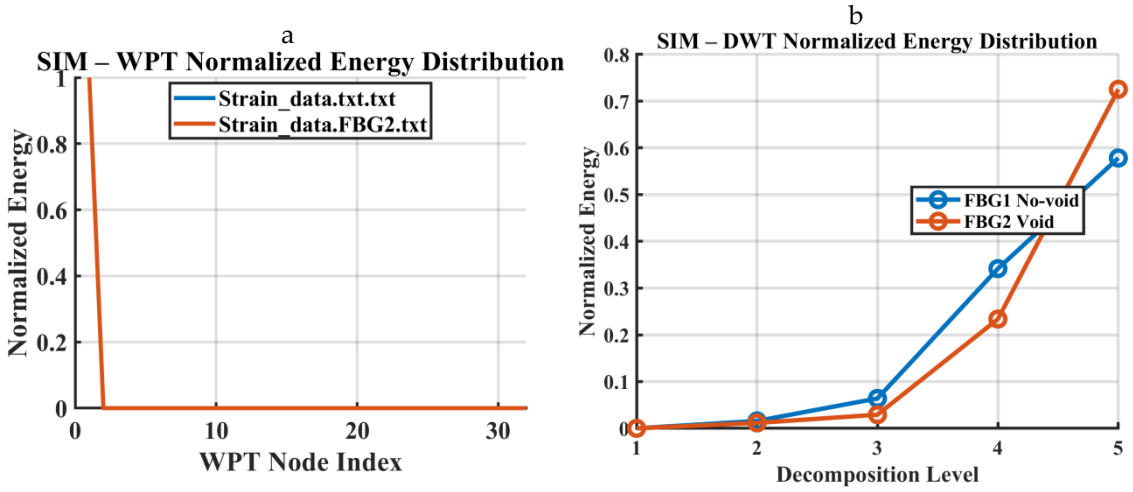

Figure 10. Numerical wavelet-energy features extracted from simulated strain responses: (a) WPT normalized energy distribution across terminal nodes, (b) DWT normalized energy distribution across decomposition levels (no-void vs void).

Overall, the simulated DWT and WPT results seems to reinforce the experimental findings and provide additional support for the physical meaning of the extracted energy-based indicators. The agreement between numerical and experimental trends suggests that void damage is more appropriately characterized as a redistribution and attenuation process in the measured strain response, rather than as a purely time-domain amplitude effect.

3.7. Statistical Validation of Selected Wavelet-Energy Features

Figure 11 and Table 1 summarize the statistical behavior of the selected DWT and WPT energy features under the no-void and void conditions. For all four features, the void condition exhibits a clear increase in mean normalized energy relative to the no-void state. This trend is consistent with the earlier multiresolution results, which showed that defect presence leads to redistribution of signal energy across wavelet scales and packet nodes. The standard deviations remain small for both structural states, indicating low within condition variability and good repeatability of the extracted

 doi:10.20944/preprints202604.0067.v1

features across repeated measurements. This suggests that the observed differences are not caused by random fluctuations alone, but reflect stable changes in the measured strain response associated with the presence of the void. The independent two-sample t-test results further confirm the statistical significance of these differences. All selected features yield p-values below 0.001, demonstrating strong statistical separation between the no-void and void conditions.

Table 1. Mean and standard deviation of selected wavelet-energy features under no-void and void conditions.

Feature	No-void Mean	No-void SD	Void Mean	Void SD	p-value
FBG1 DWT-L2	0.42	0.0158	0.514	0.023	6.76×10^{-5}
FBG1 DWT-L3	0.21	0.0158	0.28	0.0158	1.13×10^{-4}
FBG2 WPT-N1	0.55	0.0158	0.67	0.0158	2.14×10^{-6}
FBG2 WPT-N3	0.178	0.0084	0.26	0.0158	7.06×10^{-6}

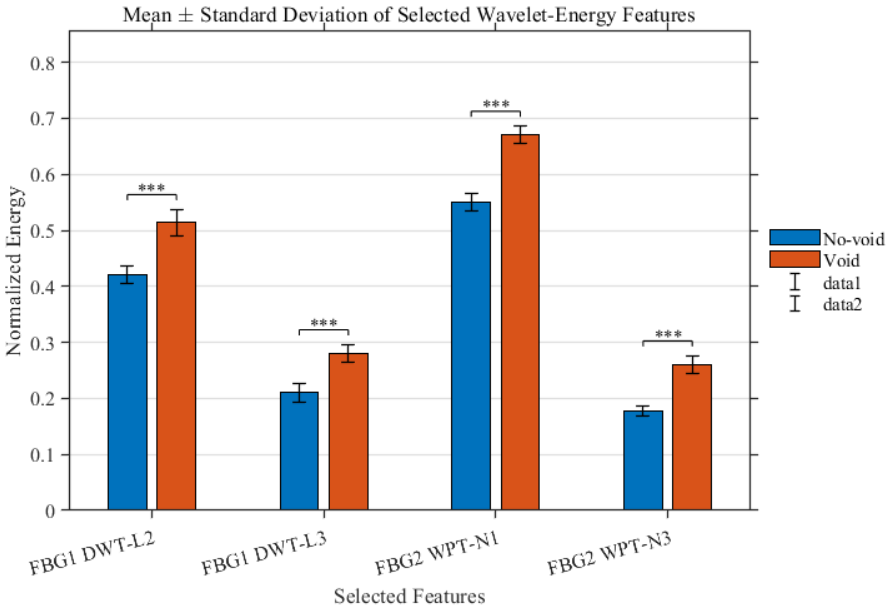

Figure 11. Mean standard deviation of selected DWT and WPT energy features for no-void and void conditions at FBG1 and FBG2. The observed shift in mean values and the limited overlap of the error bars indicate that the selected multiresolution features provide consistent discrimination between intact and defective states.

Among the selected indicators, The WPT-based features show the largest mean shifts, confirming that both coarse and fine multiresolution energy measures are effective for defect discrimination. The DWT-based features also show significant differences, confirming that both coarse and fine multiresolution energy measures are effective for defect discrimination.

Thus, the results in Figure 11 and Table 1 provide quantitative support for the discriminative capability of the proposed multiresolution wavelet-energy features. When considered together with the CWT, DWT, and WPT analyses, the statistical validation strengthens the conclusion that void damage produces consistent and measurable changes in the recorded FBG strain response.

3.8. Discussion and Implications for Pressure Vessel SHM

The combined experimental and numerical results indicate that single-FBG sensing under guided-wave excitation, when coupled with multiresolution wavelet analysis, can distinguish between void and no-void conditions in curved pressure vessel structures. The CWT scalograms provide an interpretable view of damage-related non-stationarity, while the normalized DWT and WPT energies offer quantitative indicators of structural condition. Together, these results show that

 doi:10.20944/preprints202604.0067.v1

meaningful defect-sensitive features can be extracted even when the sensing system does not directly resolve the ultrasonic carrier waveform.

From a practical SHM perspective, the proposed framework offers several advantages. First, it reduces sensing complexity relative to dense multi-sensor layouts by demonstrating that a single-channel FBG measurement can still provide useful diagnostic information under the tested configurations. Second, the extracted wavelet-energy features are physically interpretable and computationally lightweight, making them suitable for low-complexity monitoring scenarios where transparency and efficiency are important. Third, the framework does not rely on large labeled datasets or data-intensive learning models, which improves its suitability for applications where limited experimental data are available.

At the same time, the present results should be interpreted within the scope of the investigated configurations. The study demonstrates feature sensitivity to the presence of a void under specific actuator-sensor paths, rather than full defect coverage across all possible locations and geometries. Detection performance may vary with defect size, position, structural complexity, and sensing arrangement. Nevertheless, the observed consistency between experimental and numerical trends suggests that multiresolution energy redistribution provides a useful physical basis for defect discrimination in curved pressure vessel structures.

Overall, the findings support the feasibility of low-bandwidth FBG-based strain-response monitoring for practical pressure vessel SHM. The study therefore provides a foundation for future work on extended sensor layouts, multiple defect scenarios, statistical validation under broader operating conditions, and integration with higher-bandwidth or hybrid sensing systems for enhanced diagnostic coverage.

4. Conclusions

This study presented a multiresolution wavelet-energy framework for void detection in curved pressure vessel structures using single-FBG sensing under guided-wave excitation. Guided waves generated by PZT actuators were measured as strain-induced wavelength shifts by surface-mounted FBG sensors, and the resulting responses were analyzed using CWT, DWT, and WPT to extract defect-sensitive features. The experimental results showed that the presence of a void produces measurable changes in the recorded strain response, including increased non-stationarity in the time-frequency domain and systematic redistribution of energy across wavelet scales and packet nodes. The normalized DWT and WPT energy features provided compact and physically interpretable indicators that consistently distinguished the void and no-void conditions under the investigated sensing configurations. The added statistical analysis further supported the repeatability and discriminative capability of the selected multiresolution features.

Finite-element simulations reproduced the same qualitative energy redistribution trends observed experimentally, supporting the interpretation that the measured changes arise from defect-related scattering, attenuation, and mode interaction. This agreement between experiment and simulation strengthens the physical basis of the proposed sensing and analysis framework. Overall, the results demonstrate that low-bandwidth FBG measurements, when combined with multiresolution wavelet-energy analysis, can provide a practical and low-complexity means of distinguishing void and no-void conditions in curved pressure vessel structures. Although the present study is limited to specific defect and sensing configurations, it establishes a useful foundation for future work on broader defect scenarios, expanded sensor layouts, higher-bandwidth interrogation, and hybrid sensing strategies.

Declaration of Interest Statement: The author(s) declared no potential conflicts of interest with respect to the research, authorship and/or publication of this article.

Data Availability: The data that support the findings of this study are openly available and have been provided at OST: 10.17605/OSF.IO/WVRB5.

 doi:10.20944/preprints202604.0067.v1

Acknowledgments: The author(s) disclosed receipt of the following financial support for the research, authorship, and /or publication of this article: This work was supported by the Shenzhen International Cooperative Research Project (GJHZ 20240218113606013), Foreign Experts Program of the Ministry of Science and Technology (No. 6181480008) and Postgraduate Research & Practice Innovation Program of Jiangsu Province (KYCX24_3926).

References

1. Ostachowicz, W., J., Güemes. New Trends in Structural Health Monitoring. *CISM International Centre for Mechanical Sciences* 2013; DOI 10.1007/978-3-7091-1390-51.
2. Ohtsuka, N., Nakano M., & Ueyama, H. Acoustic emission monitoring during rupture test of pressure vessel and laboratory fracture test. *Journal Pressure Vessel Technology* 1981;103(2): 191-199.
3. Liu, Z., Mu W., Ning H., Wu M., & Liu, G. Pressure vessel leakage detection method based on online acoustic emission signals. The British Institute of Non-Destructive Testing. *Non-Destructive Testingand Condition Monitoring* 2023; https://doi.org/ 10.1784 /insi. 2023.65.1.36.
4. Wang ZP, Fei Y, Qian L, et al. Non-contact detecting impact damage location for composite plate based on HHT. *Rare Metal Mat Eng* 2021; 50(2): 469-474.
5. Yao, X., F., Meng, L., B., Jin, J.C. & Yeh, H., Y. Full-field deformation measurement of fiber composite pressure vessel using digital speckle correlation method. *Polym Test* 2005; 24: 245-251.
6. Ennaceur, C., A. Laksimia, C., Herve' & Cherfaoui, M. Monitoring crack growth in pressure vessel steels by the acoustic emission technique and the method of potential difference. *Int. J. Pressure Vessel Piping* 2006; 83(3): 197-204.
7. Ai, Q., C., X., Liu, X., R., Chen, P., & Wang, Y. Acoustic emission of fatigue crack in pressure pipe under cyclic pressure. *Nucl. Eng. Des.* 2010; 240: 3616-3620.
8. Máthis, K., D., Prchal, R., Novotny, & Hahner, P. Acoustic emission monitoring of slow strain rate tensile tests of 304L stainless steel in supercritical water environment. *Corros. Sci.* 2011; 53: 59-63.
9. Sang S, Xu C, Wang ZP et al. Accurate prediction of topology of composite plates via machine learning and propagation of elastic waves. *Compos Commun* 2023; 37, https://doi.org/101016 /j.coco.2022.101465.
10. Zhang J., Hu, C., Yan J., Hu Y., Gao, Y., & Xuan, F. Guided Wave Damage Location of Pressure Vessel Based On Optimized XCM Neural *Network. Journal of Pressure Vessel Technology-transactions of The Asme* 2023.
11. Memmolo V., Maio, L., & Ricci, F. Assessment of Damage in Composite Pressure Vessels Using Guided Waves. *Sensors* 2022.
12. Wang Z., Chen S., Xu F., Liu, Y., & Wei M. On the application of IoT: Monitoring of pressure vessel structure. *Frontiers of Civil Engineering and Disaster Prevention and Control* 2023; ISBN9781003348436.
13. Wang ZP, Xiong XQ, Qian L, et al. Research on the progress of interdigital transducer (IDT) for structural damage monitoring. *J Sensors* 2021; https://doi.org/10.1155/2021/6630658.
14. Ciminello, M., Sikorski, B., Galasso B., Pellone, L., Mercurio, U., Concilio A., Apuleo, G., Cozzolino, A., Kressel I., Shoham, S., & Tur, M. Preliminary Results of a Structural Health Monitoring System Application for Real-Time Debonding Detection on a Full-Scale Composite Spar, *Sensors* 2023; pp.455.
15. Staszewski, W., J. Ultrasonic Guided Waves for Structural Health. *Ltrasonic* 2005; 09-15ISSN1662-9795: doi: 10.402 KEM. 293 29 4.
16. Mitra, M., & Gopalakrishnan, S. Guided wave based structural health monitoring: A review, *Smart Mater. Struct;* 2016: 053001.
17. Rose, J. L. Ultrasonic Guided Waves in Solid Media. *Cambridge University Press* 2014.
18. Giurgiutiu, V. Structural Health Monitoring with Piezoelectric Wafer Active Sensors. *Academic Press* 2008.
19. Raghavan, A., Cesnik, C. E. S. Review of guided-wave structural health monitoring. Shock and Vibration Digest 2007.
20. Soman, R.; Wee, J.; Peters, K. Optical Fiber Sensors for Ultrasonic Structural Health Monitoring: A Review. Sensors 2021, 21(21), 7345.
21. Soman, R. Multi-objective optimization for joint actuator and sensor placement for guided waves based structural health monitoring using fibre Bragg grating sensors. Ultrasonics 2022, 119, 106605.

 doi:10.20944/preprints202604.0067.v1

22. Soman, R.; Omidi Moaf, F.; Fiborek, P.; Kudela, P.; Kurpińska, M. Investigating the suitability of the matched fiber Bragg grating approach for guided wave based structural health monitoring. Measurement 2025, 243, 115935.
23. Soman, R.; Omidi Moaf, F.; Fiborek, P.; Kudela, P.; Kurpińska, M. Investigating the suitability of the matched fiber Bragg grating approach for guided wave based structural health monitoring. Measurement 2025, 243, 115935.
24. Alhussein, A.N.D.; et al. Fiber Bragg Grating Sensors: Design, Applications, and Comparison with Other Sensing Technologies. Sensors 2025, 25(7), 2289.
25. Sun, X.; Guo, C.; Yuan, L.; Kong, Q.; Ni, Y. Diffuse Ultrasonic Wave-Based Damage Detection of Railway Tracks Using PZT/FBG Hybrid Sensing System. Sensors 2022, 22, 2504.
26. Su, Z., Ye, L. Identification of Damage Using Lamb Waves. *Springer* 2009.
27. Lowe, M. J. S. Guided waves for inspection of pipes and pressure vessels. *Ultrasonics* 2002.
28. Daubechies, I. Ten Lectures on Wavelets. *SIAM* 1992.
29. Peng, Z., Chu, F. Wavelet packet transform for fault diagnosis. *Mechanical Systems and Signal Processing* 2004.
30. Rafiee, J. Rafiee, M. A and Tse, P. W. Wavelet basis selection for rotating machinery fault diagnosis. *Expert Systems with Applications* 2009; 36(3):4862–4875.
31. Hu, C.; Yang, B.; Xiao, B.; Xuan, F.-Z.; Xiang, Y. Damage localization in pressure vessel using guided wave-based techniques: Optimizing the sensor array configuration to mitigate nozzle effects. Applied Acoustics 2022, 185, 108393.
32. Bouhala, L.; Polesel, J.; Karatrantos, A.; Perbal, S.; Senf, B.; Hiekel, A.; Reinhardt, H.; Rauscher, A.; Mäder, T. Review of State-of-the-art of structural health monitoring in hydrogen composite pressure vessels. Composites Part C: Open Access 2025, 18, 100635.
33. Kuebutornye N, Wang Z, Zhang J, Shang D, Xia Q. Mechanism of Ultrasonic Guided Wave Excitation and Sensing in Pressure Vessel Structures Under Boundary Condition Effects [J]. e-Journal of Nondestructive Testing (NDT.net), 2025-01: (NDT.net), 2025. https://doi.org/10.58286/306062
34. Mallat, S. A theory for multiresolution signal decomposition: The wavelet representation. *IEEE Transactions on Pattern Analysis and Machine Intelligence* 1989;vol. 11(7): 674–69.
35. Torrence, C. & Compo G. P. A practical guide to wavelet analysis. *Bulletin of the American Meteorological Society* 1998; 79 (1): 61–78.
36. Coifman, R. R., and Wickerhauser, M. V. Entropy-based algorithms for best basis selection. *IEEE Transactions on Information Theory* 1992; 38(2), 713–718.